Appl. Phys. A 69 [Suppl.], S99–S107 (1999) / Digital Object Identifier (DOI) 10.1007/s003399900305

Applied Physics A
Materials
Science & Processing

The role of electron–phonon coupling in femtosecond laser damage of metals

S.-S. Wellershoff, J. Hohlfeld, J. Güdde, E. Matthias

Fachbereich Physik, Freie Universität Berlin, Arnimallee 14, 14195 Berlin, Germany

Received: 21 July 1999/Accepted: 1 September 1999/Published online: 22 December 1999

Abstract. Femtosecond laser pulses were applied to study the energy deposition depth and transfer to the lattice for Au, Ni, and Mo films of varying thickness. The onset of melting, defined here as damage threshold, was detected by measuring changes in the scattering, reflection and transmission of the incident light. Experiments were done in multi-shot mode and single-shot threshold fluences were extracted by taking incubation into account. Since melting requires a well-defined energy density, we found the threshold depends on the film thickness whenever this is smaller than the range of electronic energy transport. The dependence of the threshold fluence on the pulse length and film thickness can be well described by the two-temperature model, proving that laser damage in metals is a purely thermal process even for femtosecond pulses. The importance of electron–phonon coupling is reflected by the great difference in electron diffusion depths of noble and transition metals.

PACS: 78.47.+p; 79.20.Ds; 72.15Eb

It is well known that using subpicosecond pulses in laser ablation has two major advantages over using nanosecond pulses: much lower fluences are needed to accomplish ablation [1–5] and considerably sharper contours can be achieved [2, 6–8]. The latter is illustrated in Fig. 1 for stainless steel[1]. Figure 1a shows a hole produced with 248-nm, 25-ns pulses, and Fig. 1b presents one obtained with 120-fs pulses of the same wavelength. The precision of the lower edge is magnified in Fig. 1c. Obviously, melting and debris contamination greatly reduce the quality of microstructures that can be achieved with nanosecond pulses. For such pulses thermal energy diffusion into deeper parts of the material takes place during excitation, which reduces the energy density near the surface and broadens the energy distribution. The diffusive energy transport can be truncated by using metal films with thickness smaller than the diffusion length. This effect was shown for nanosecond pulses and the decrease of ablation threshold with film thickness was described by the thermal diffusion model [9–11].

In this paper we want to show that also for femtosecond laser pulses there is diffusive energy transport by hot electrons as long as there is no thermal equilibrium between electrons and phonons [4, 12–14]. The resulting electron thermal diffusion length is the decisive quantity for fs-laser material processing, determining both the damage threshold and the structure sharpness. Corkum et al. [15] were the first to point out that the range of electronic thermal diffusion is determined by the electron–phonon coupling strength. On the basis of the two- temperature model they calculated the electronic diffusion range and defined a critical pulse duration τ_c, which separates the ultrashort and ns ablation regimes. It is important to note, however, that diffusion of hot electrons presupposes the existence of an electron temperature brought about by collisions of excited electrons with those near the Fermi level [16–19]. The time to convert the initially highly non-equilibrium electrons into a thermal distribution depends, therefore, on excitation energy and density of states (DOS) at the Fermi level. Consequently, the conversion takes much longer for noble metals than for transition metals.

Before an electron temperature is established, the non-equilibrium electrons penetrate into the material with ballistic velocities of the order of 10^6 m/s in the case of Au [19–21]. Accordingly, the ballistic range can reach 100 nm for 100-fs pulses. In transition metals with large *d*-band densities, this is of the order of the optical penetration depth. Hence, when considering the transport of absorbed energy into the depth of the material we have to distinguish three processes occurring in successive time intervals, as sketched in Fig. 2. The first process is the highly non-equilibrium state of excited electrons which relax by electron– electron ($e-e$) collisions. The duration of this phase is determined by the collision rate, governed by the DOS at the Fermi level. The second interval is

[1] The authors thank Dipl.-Ing. G. Herbst, Fimea GmbH, Berlin-Adlershof, for his permission to publish these results.

COLA'99 – 5th International Conference on Laser Ablation, July 19–23, 1999 in Göttingen, Germany

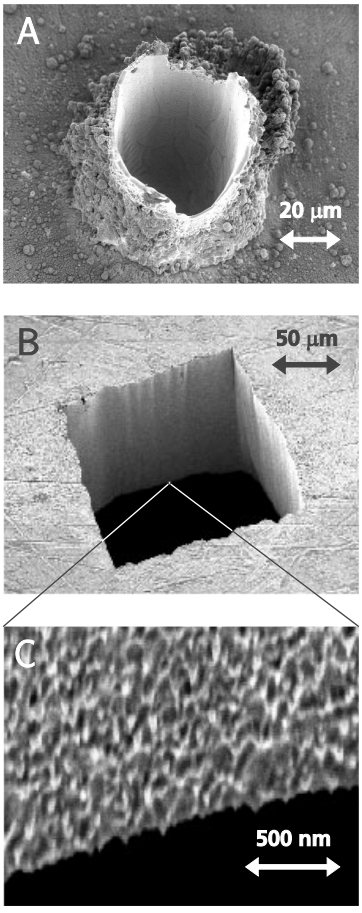

Fig. 1a–c. Microstructuring of a stainless steel sheet with 248-nm laser radiation. **a** A hole drilled with 25-ns pulses and a fluence of about 8 J/cm^2. **b** A rectangular hole cut with 120-fs pulses at 1×10^{13} W/cm^2. **c** A magnified picture of the exit edge in **b**. These ablation structures were produced by G. Herbst, Fimea GmbH, Berlin

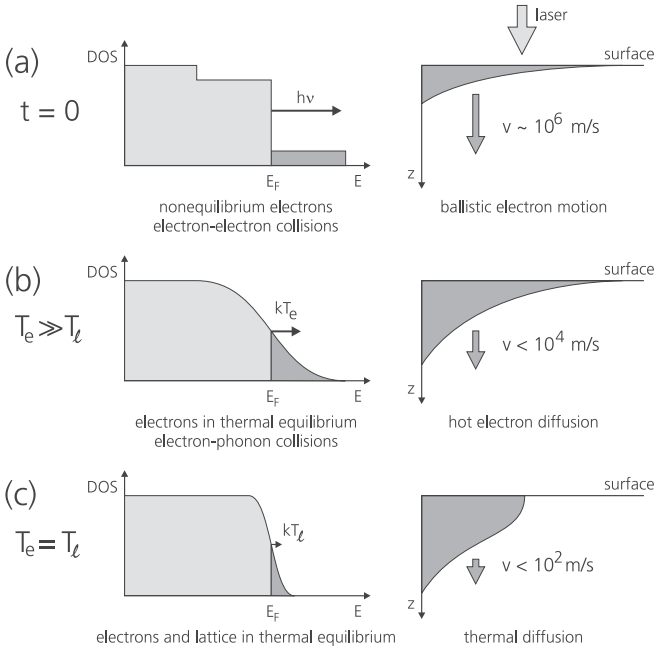

Fig. 2a–c. Relaxation phases following optical excitation of metals. At $t = 0$ a highly non-equilibrium state is generated (**a**) which deexcites by $e-e$ collisions to form an electron temperature (**b**). This, in turn, cools by $e-ph$ interaction until it reaches thermal equilibrium with the lattice (**c**). The energy distributions inside the material and transport velocities are indicated on the right

characterized by the existence of a Fermi distribution and the diffusion of hot electrons driven by the temperature gradient. The hot-electron bath cools by electron–phonon ($e-ph$) interaction, the strength of which limits the diffusion range. The final state is reached when electrons and the lattice are in thermal equilibrium, where the common thermal diffusion drives the heat dissipation into the material.

The range of heat diffusion prevents sharp microstructural contours and constitutes an energy-loss mechanism. This was discussed at the COLA'93 meeting and elsewhere [9–11] for nanosecond laser pulses, where electrons and lattice are in thermal equilibrium. Here, we will treat the energy deposition depth for subpicosecond pulses where the electrons and lattice are out of equilibrium. Although rate-equation models have been proposed to describe the initial redistribution of the absorbed energy [19, 20], we will show that the two-temperature model (TTM) [22] can be successfully applied to predict threshold fluences for melting. Even the ballistic motion can be incorporated into the TTM by altering the source term [13, 14]. The crucial parameter is the $e-ph$ coupling constant, g, which determines the range of hot-electron diffusion and thereby governs both the energy loss into the material and the zone of thermal damage. In accordance with their different g values, we find vastly different energy deposition ranges for noble and transition metals. Once the metal film thickness is smaller than this range, the fluence threshold decreases again linearly with thickness, since the critical energy density required for melting remains constant.

1 Two-temperature model

As soon as an electron temperature is established, the TTM [22] can be applied to describe the temperature dynamics. It consists of the diffusion equations for the electrons and lattice, coupled by a term proportional to the temperature difference of the two reservoirs multiplied by the strength of the electron–phonon interaction:

$$C_e\left(T_e\right)\frac{\partial T_e}{\partial t} = \nabla\left(K_e \nabla T_e\right) - g\left(T_e - T_l\right) + S\left(z,t\right) \tag{1}$$

$$C_l\frac{\partial T_l}{\partial t} = \nabla\left(K_l \nabla T_l\right) + g\left(T_e - T_l\right)\ , \tag{2}$$

where C and K are the heat capacities and thermal conductivities of the electrons and lattice as denoted by the subscripts e and l. The source term $S\left(z,t\right)$ contains the absorbed energy and will be discussed in Sect. 1.3. Since in metals the thermal conduction is dominated by electrons, we neglected the diffusion term for the lattice in (2).

1.1 Diffusion depth for nanosecond pulses

In the nanosecond pulse regime the electrons and lattice are in thermal equilibrium, $T_e = T_l$. Hence, the dependence on the

$e-ph$ coupling strength vanishes, and (1) and (2) reduce to the usual heat diffusion equation:

$$C\frac{\partial T}{\partial t} - K\nabla^2 T = S\,(z,t)\ . \tag{3}$$

The solution for pulsed excitation has been frequently discussed in the literature (see, e.g., [11, 14, 23, 24]). For a δ-function pulse in time and an absorbed fluence, $F_{\rm abs}$, in a surface layer at $z = 0$, one finds for $t > 0$ a temperature increase $\Delta T = T - T_0$:

$$\Delta T_\delta\,(z,t) = \frac{F_{\rm abs}}{C\sqrt{\pi Dt}}\exp\left(\frac{-z^2}{4Dt}\right)\ , \tag{4}$$

where $D = K/C$ is the diffusivity of the material. This temperature distribution decays rapidly in time and spreads into the material with a thermal diffusion length $L_{{\rm th},\delta} = \sqrt{\pi Dt}$. For Gaussian pulses, (3) must be solved numerically and one finds that the thermal diffusion length is $L_{{\rm th},T\,\max} = \sqrt{2D\tau}$ at the time when the lattice temperature has reached its maximum at the surface, i.e., when damage occurs. The time τ is defined as the half width at half maximum of the laser pulse, $\tau = \tau_L/2$ [14, 25].

Figure 3a illustrates the diffusive temperature spread in gold during the first 100 ns after excitation by a Gaussian pulse of $\tau_L = 25$ ns and an absorbed fluence of $F_{\rm abs} = 130\,{\rm mJ/cm^2}$. Taking into account ballistic transport [19–21], the calculation assumed an initial energy distribution of

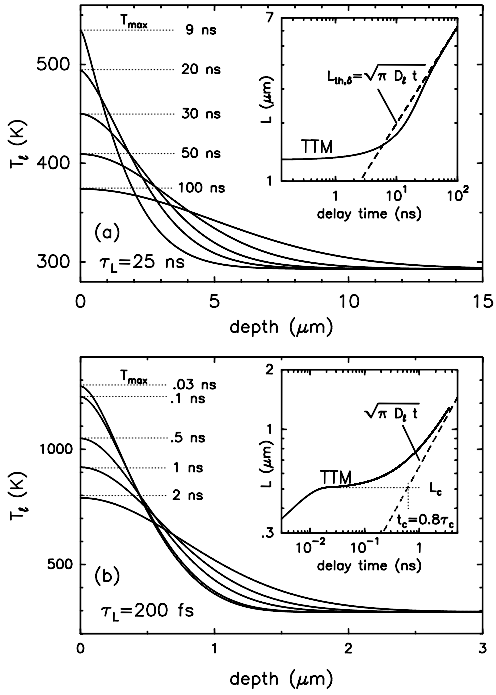

Fig. 3a,b. Lattice temperature distributions at certain times after excitation of a Au bulk sample by Gaussian pulses of $\tau_L = 25$ ns (**a**) and 200 fs (**b**) with a fluence of $130\,{\rm mJ/cm^2}$. The *curves* show the time evolution of the spatial distributions in intervals given by the numbers in nanoseconds. The *insets* show the time dependencies of the thermal diffusion lengths calculated with the full TTM for a Gaussian pulse and finite absorption depth (*solid lines*) and from the solution (4) for δ-function excitation. The range of electron diffusion is given by $L_{\rm c}$ (see Sect. 1.4)

120 nm. Note the deep penetration of the temperature distribution into the material. The profiles in Fig. 3a can be scaled up to higher fluences and provide an impression of the thermal damage zone when microstructuring metal with nanosecond laser pulses. The inset shows the time development of the thermal diffusion length and compares results of TTM calculations for Gaussian pulses (solid line) with the δ-pulse approximation (dashed line). One recognizes that for $t \geq 2\tau_L$ both curves become identical and the diffusion length is given by $L_{{\rm th},\delta} = \sqrt{\pi Dt}$.

The consequence of thermal diffusion is that for materials thicker than $L_{th,T\max}$, only a fraction of the absorbed energy remains near the surface and contributes to melting and evaporation. This energy transport to deeper parts of the sample is ignored when using the total absorbed energy density $F_{\rm abs}\alpha$ to define the damage threshold (α is the absorption constant). Instead, damage results when $F_{\rm abs}/L_{{\rm th},T\,\max}$ exceeds the critical energy density required for the phase transition. For films with thickness $d < L_{{\rm th},T\,\max}$, diffusion is blocked and, at constant fluence, the energy density increases with decreasing d. Accordingly, the threshold fluence for damage decreases with d, as shown in [9–11].

1.2 Excitation with femtosecond pulses

For excitation with ultrashort pulses, the term $g\,(T_{\rm e} - T_{\rm l}) > 0$ in (1) and (2) determines cooling of the electron bath after it has reached thermal equilibrium as defined by a Fermi distribution (Fig. 2). The influence of hot-electron diffusion on the lattice temperature distribution is displayed in Fig. 3b for a few time intervals after excitation of Au with one 200-fs pulse with an absorbed fluence of $130\,{\rm mJ/cm^2}$. Compared to the case with nanosecond pulses, the thermal diffusion range is much shorter and the maximum lattice temperature at the surface, reached 30 ps after excitation, approaches the melting temperature. The thermal damage zone would shrink accordingly when Au is processed with femtosecond laser pulses. In the inset of Fig. 3b we again compare the time variation of the diffusion length for δ-function excitation with the one calculated by the TTM for a Gaussian pulse and a 120-nm absorption depth. As a consequence of the $e-ph$ coupling we observe at about 30 ps the onset of a plateau which corresponds to the diffusion range $L_{\rm c}$ of hot electrons, as discussed in Sect. 1.4. The critical pulse duration $\tau_{\rm c}$, which separates the ultrashort-pulse regime governed by $L_{\rm c}$ from the ns ablation governed by $L_{{\rm th},T\,\max}$ can be derived from $L_{\rm c} = L_{{\rm th},T\,\max} = \sqrt{2D\tau_{\rm c}}$ (see Sect. 1.5).

Relaxation patterns predicted by the TTM for 100-nm Au and Ni films are shown in Fig. 4; they assume absorption of 200-fs, 400-nm pulses of $23\,{\rm mJ/cm^2}$. The absorbed energy density was chosen to reach the melting points of the lattices. The electron and lattice temperatures at the front and rear surfaces of the films are plotted in both cases. The curves are typical for noble and transition metals. The transfer of energy to the lattice proceeds about ten times faster for Ni because of the much larger $e-ph$ coupling constant (see Table 1). There is no significant heat transport through the Ni film to the rear surface, where the temperature barely changes even though the front surface reaches the melting point.

The opposite is true for noble metals with weak $e-ph$ coupling, as can be seen in Fig. 4 for Au. The lattice temperature rise at the front surface is much slower since most

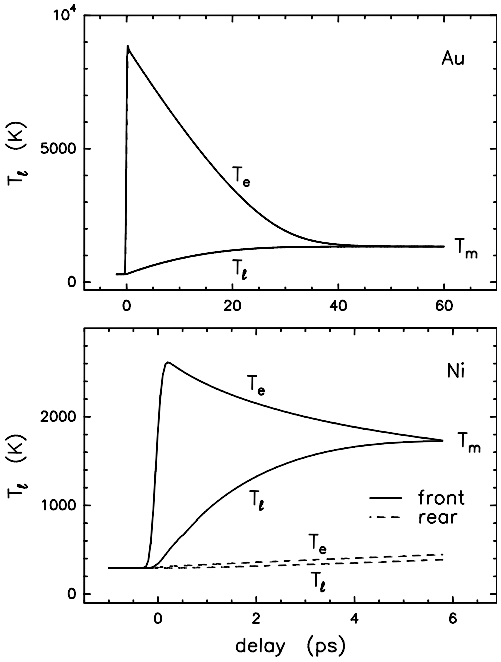

Fig. 4. Time dependence of electron and lattice temperatures predicted by the two-temperature model for 100-nm Au and Ni films irradiated with a single 200-fs, 400-nm laser pulse at a fluence of 23 mJ/cm^2. The temperatures at the front (*solid lines*) and rear (*dashed lines*) sides of the films are plotted, which are indistinguishable for the Au film but very different for Ni. The upper time scale for Au differs by nearly a factor of ten from the lower one for Ni

of the absorbed energy is transported into the interior of the metal. Using the same fluence, it takes 10 times longer for the Au than for the Ni film to reach the melting point. The quick spread of absorbed energy throughout the entire film is proven by the fact that we barely see any difference between the lattice temperature at the front and rear surfaces of the Au film. This demonstrates that microstructuring is much more efficient in metals with strong $e-ph$ coupling.

1.3 The source term

As illustrated in Fig. 2, the first phase after photon absorption is ballistic motion of non- equilibrium electrons [13, 14, 19–21]. For transition metals the ballistic range is of the order of the optical absorption depth. For noble metals with a much smaller $e-e$ collision rate, however, the ballistic transport depth is significant and must be taken into account. Figure 5 demonstrates its influence on electron temperature relaxation at the surface of Au films. Examples are presented for thickness smaller than, equal to, and larger than the ballistic range of 100 nm. The electron temperature was generated by 400-nm, 200-fs pump pulses and probed by the transient reflectivity of 500-nm, 100-fs probe pulses. At 500 nm the reflectivity is proportional to the electron temperature [13, 14]. The dashed lines are calculated by the TTM and overestimate T_e for short times, except for the 20-nm film. The experimental data prove that the energy density is lower than expected from absorption whenever ballistic transport takes place. This can be taken into account by introducing an effective initial absorption depth into the source term of (1) [13, 14], consisting of the sum of the optical absorption depth $\lambda_0 = \alpha^{-1}$ and

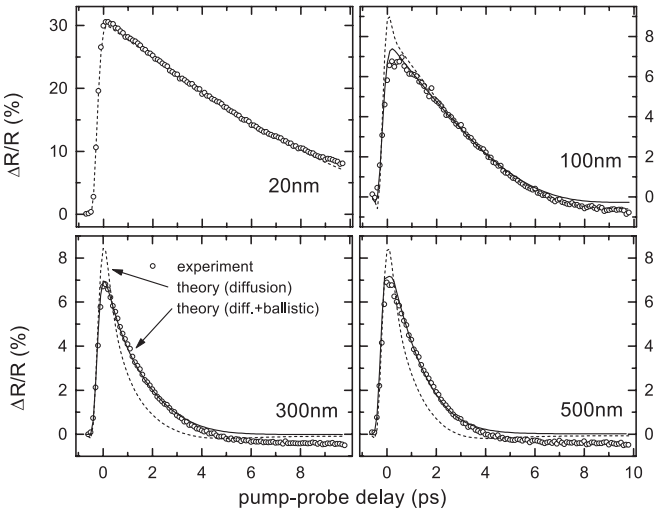

Fig. 5. Comparison of experimental transient reflectivities [14] with predictions of the two-temperature model for Au films of thickness smaller than, equal to, and larger than the ballistic range of 100 nm. The data were measured in pump–probe mode with 400-nm, 200-fs pump pulses of 1 mJ/cm^2 and *p*-polarized probe pulses of 500 nm and 100 fs. *Solid lines* represent TTM calculations taking into account the ballistic penetration depth; *dashed lines* ignore this correction

the ballistic range λ_{ball}. This leads to a modified source term:

$$S(z,t) = I(t)\,(1-R-T) \times \frac{\exp\left(-z/(\lambda_0+\lambda_{\text{ball}})\right)}{(\lambda_0+\lambda_{\text{ball}})\left(1-\exp\left(-d/(\lambda_0+\lambda_{\text{ball}})\right)\right)}\,. \qquad (5)$$

When this expression is applied, the solid lines fit the experimental data perfectly up to about 4 ps for $\lambda_{\text{ball}} = 105$ nm. This range is in agreement with the results reported in [21]. Deviations between the measured results and TTM predictions for times longer than 4 ps are caused by slight changes in the band structure with increasing lattice temperature which, in turn, affects the reflectivity. The phenomenological character of the TTM is unable to incorporate such effect.

The effective energy deposition depth following optical absorption and spreading by ballistic transport will from now on be included in the source term of all TTM calculations for Au films.

1.4 Electron diffusion length

Figure 4 shows that the equilibration time for electrons and the lattice depends on the $e-ph$ coupling constant, thereby determining the diffusive penetration depth of the electrons. Corkum et al. [15] gave estimates of these two quantities in terms of the thermal constants of the material. This will briefly be recapitulated here. One uses the approximation that electronic heat transport proceeds almost unhindered by electron–phonon interaction for a time τ_R until a crucial length L_c is reached, beyond which equilibrium thermal diffusion takes over. With this assumption, an estimate of L_c and τ_R can be found from the diffusion equation for electrons only. By neglecting the $e-ph$ coupling term and introducing the relations [14] $C_e = A_e T_e$ and $K_e = K_{e,0} T_e/T_l$, we change (1) into a diffusion equation for T_e^2:

$$A_e \frac{\partial}{\partial t}\left(T_e^2\right) = \frac{K_{e,0}}{T_l}\frac{\partial^2}{\partial z^2}\left(T_e^2\right) + 2S(z,t)\,. \qquad (6)$$

The constants $K_{e,0}$ and A_e describe properties of the electrons such as the density, Fermi energy, effective mass, and electron–phonon collision rate. Analogous to (4), the solution of (6) is [14, 15]

$$T_e^2(z,t) = \frac{2F_{\mathrm{abs}}}{A_e}\sqrt{\frac{A_e T_l}{\pi K_{e,0} t}}\exp\left(\frac{-A_e T_l z^2}{4K_{e,0}t}\right). \quad (7)$$

From this expression one can define the critical length for the diffusion of electrons:

$$L_{\mathrm{c}} = \sqrt{\frac{2K_{e,0}}{A_e T_l}\tau_R}, \quad (8)$$

where $\tau_R = A_e T_e(z=0,\tau_R)/g$ is the electron–phonon relaxation time.

Since we are concerned with melting, it is desirable to express the crucial length in terms of the melting temperature T_{m}. Substituting the absorbed fluence by the threshold fluence for melting, $F_{\mathrm{abs}} \equiv F_{\mathrm{th}} = C_l T_{\mathrm{m}} L_{\mathrm{c}}$, we obtain an expression which relates the electronic diffusion length to the melting temperature and $e-ph$ coupling strength [14, 15]:

$$L_{\mathrm{c}} = \left(\frac{128}{\pi}\right)^{1/8}\left(\frac{K_{e,0}^2 C_l}{A_e T_{\mathrm{m}} g^2}\right)^{1/4}. \quad (9)$$

The importance of this relation is that the dependence of the threshold fluence on the film thickness changes dramatically when the thickness d exceeds L_{c}, as will be shown in Sect. 2.1.

1.5 Electron–phonon energy transfer time

An analogous expression for the electron–phonon relaxation time is found by combining (8) and (9), leading to:

$$\tau_R = \left(\frac{8}{\pi}\right)^{1/4}\left(\frac{A_e T_{\mathrm{m}} C_l}{g^2}\right)^{1/2}. \quad (10)$$

It was pointed out by Corkum et al. [15] that the critical pulse duration τ_{c}, beyond which the threshold fluence shows the usual $\sqrt{2D\tau}$ dependence, discussed for nanosecond pulses in Sect. 1.1, can be derived from the condition $L_{\mathrm{c}} = L_{\mathrm{th},T\max}$. Using (9), one finds the following expression [15]:

$$\tau_{\mathrm{c}} = \left(\frac{8}{\pi}\right)^{1/4}\left(\frac{C_l^3}{A_e T_{\mathrm{m}} g^2}\right)^{1/2}. \quad (11)$$

2 Comparison with experimental results

Laser-induced damage is defined here as melting of the surface. It can be detected either in situ by observing changes of optical properties like reflection, scattering, and transmission [4, 12] or later on by scanning electron microscopy [2, 3, 6, 7]. To start the melting process, the absorbed energy density has to match the critical value $C_l(T_{\mathrm{m}} - T_0)$. Assuming $T_0 \ll T_{\mathrm{m}}$, melting requires a threshold fluence $F_{\mathrm{th}} = C_l T_{\mathrm{m}} L_{\mathrm{c}}$, which can be rewritten by inserting (9) [14]:

$$F_{\mathrm{th}} = \left(\frac{128}{\pi}\right)^{1/8}\left(\frac{K_{e,0}^2 C_l^5 T_{\mathrm{m}}^3}{A_e g^2}\right)^{1/4}. \quad (12)$$

This formula provides the desired link between the *absorbed* laser fluence, the melting temperature, and the $e-ph$ coupling strength.

2.1 Damage thresholds for Au *films*

The threshold fluences of Au films have been investigated by Stuart et al. [3] as a function of both film thickness and pulse length by using 1053-nm laser pulses. In our laboratory we studied the melting threshold with 400-nm, 200-fs pulses as a function of the film thickness [4, 12, 14]. The different photon energies imply that Stuart et al. excited only *s* electrons, whereas we also excited *d* electrons. We will first discuss the pulse length dependence obtained by Stuart et al., covering the range from 140 fs to 1 ns. Their results for a 200-nm Au grating have been replotted in Fig. 6. Each data point originates from typically 600 shots on one spot and the damage threshold was detected by scanning electron microscopy [3]. The shaded band represents a TTM fit to the data that uses the Au thermal constants listed in Table 1, including their uncertainties, and takes into account transient absorption due to a change of reflectivity with electron temperature [13, 14]. The dashed line shows the result of the same TTM calculation, but with constant absorption. The good agreement between experimental data and the TTM prediction for transient

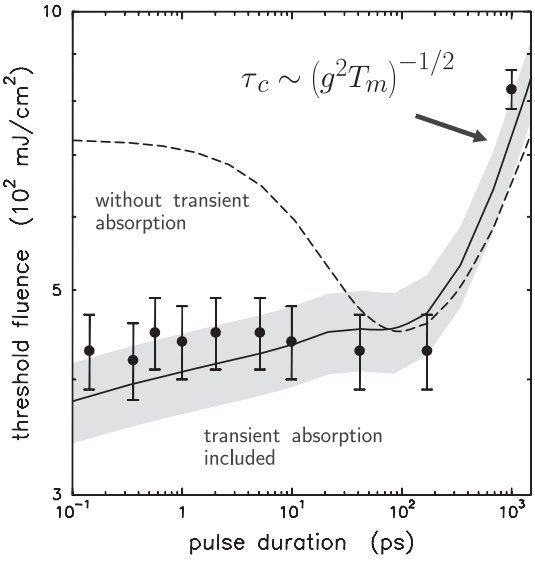

Fig. 6. Pulse length (FWHM) dependence of melting threshold fluences measured by Stuart et al. [3] on a 200-nm - thick Au grating with 1053-nm pulses. The *shaded band* results from the two-temperature model, including uncertainties in the constants and the transient change of reflectivity with electron temperature. The *dashed line* results from TTM calculations based on constant absorption. The *arrow* indicates the time τ_{c} (see (11)), beyond which heat transport proceeds with equilibrium thermal diffusion, proportional to $\sqrt{\tau_L}$

Table 1. Material constants used for TTM calculations. The values for electron–phonon coupling constant g are for Ni and Mo from [12] and for Au from [13]. Thermal conductivities $K_{e,0}$ at $T = 273\,\mathrm{K}$ are taken from [27], lattice heat capacities C_l at $T = 300\,\mathrm{K}$ are from [28]. The specific heat constants A_e for Au and Ni are copied from [27], while the value for Mo was obtained from the fit

metal	g	A_e	$K_{e,0}$	C_l	T_m
	$(10^{16}\,\mathrm{W\,m^{-3}\,K^{-1}})$	$(\mathrm{J\,m^{-3}\,K^{-2}})$	$(\mathrm{W\,m^{-1}\,K^{-1}})$	$(10^{6}\,\mathrm{J\,m^{-3}\,K^{-1}})$	(K)
Au	2.1	71	318	2.5	1337
Mo	13	350	135	2.8	2896
Ni	36	1065	91	4.1	1728

absorption proves the applicability of the model and emphasizes the necessity to include the transient character of the reflectivity for short times. Our fit, represented by the solid line in Fig. 6, yields $g = 2.2 \times 10^{16}\,\mathrm{W\,m^{-3}\,K^{-1}}$, whereas Stuart et al. [3] report $g = 35 \times 10^{16}\,\mathrm{W\,m^{-3}\,K^{-1}}$, which strongly deviates from literature values, which scatter in the range $(2-4) \times 10^{16}\,\mathrm{W\,m^{-3}\,K^{-1}}$ [12].

In Fig. 6 an arrow indicates the time τ_c, the beginning of heat diffusion in thermal equilibrium, scaling with $\sqrt{\tau_L}$, as discussed in Sect. 1.1. Note that τ_c scales with g^{-1}, therefore the deviation from $\sqrt{\tau_L}$ would occur at shorter pulse lengths for transition metals with their larger $e-ph$ coupling.

For laser microstructuring with high precision, the thermal damage zone is of interest. For this reason we kept the pulse length constant and varied the thickness [4, 12] to investigate the electronic diffusion length (defined in Sect. 1.4). We measured melting thresholds by observing changes in scattering, reflection, and transmission of the laser light during multi-shot irradiation of one spot in air at room temperature. Incubation effects were accounted for by extrapolating multi-shot threshold fluences to single-shot values by utilizing the procedure proposed by Jee et al. [26]. The thickness dependence of the melting thresholds of Au films on fused silica substrates obtained in this way is displayed in Fig. 7[2]. The solid line is a fit of the TTM to the data with the parameters listed in Table 1. The calculations included transient changes in absorption, as discussed in connection with Fig. 6. Three facts emerge from Fig. 7 as follows. (1) For thicknesses larger than 800 nm, the melting threshold saturates around $115\,\mathrm{mJ/cm^2}$, i.e., the sample is thick compared to the electronic diffusion range. (2) For films thinner than $L_c = 443\,\mathrm{nm}$ the threshold fluence increases *linearly* with thickness. As an example, the melting fluence differs by a factor of ten (!) between a 10-nm film and a 500-nm one. This observation carries the message that films with thickness $d < L_c$ can be structured with greater precision, and less energy per pulse is required for the process. (3) The ordinate offset at zero film thickness is interpreted as the melting enthalpy, which is treated here as a fit parameter.

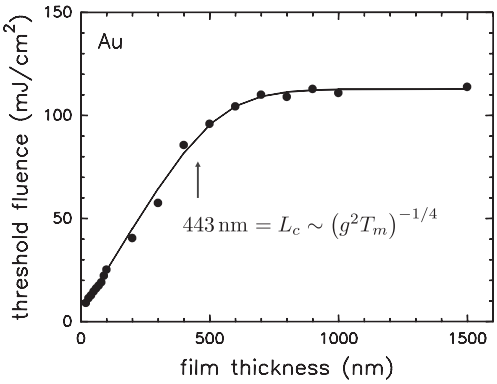

Fig. 7. Dependence of threshold fluences on the film thickness of Au films, measured with 200-fs, 400-nm pulses by recording changes in the scattering, reflection, and transmission at the melting point in multi-shot mode, as reported in [12]. Single-shot fluences obtained by correcting for incubation following the recipe of Jee et al. [26] are plotted. The *solid line* is a fit of the data by TTM with the parameters listed in Table 1. The *arrow* marks the range of hot-electron diffusion before the electrons and lattice reach thermal equilibrium

2.2 *Damage thresholds of* Ni *and* Mo *films*

The importance of $e-ph$ coupling for laser processing can be demonstrated by studying the melting thresholds of transition-metal films. As examples, we used Ni and Mo films on fused silica substrates (see also [12]). Figure 8a shows the raw data for a 100-nm Ni film taken in air at room temperature. Changes in scattering, reflection, and transmission were measured with 400-nm, 200-fs pulses as a function of the incident fluence. The fluence scan was recorded in multi-shot mode at one spot, and each fluence step in Fig. 8a was accumulated for 7500 laser shots.

There is a dramatic change in the scattered light intensity around $22\,\mathrm{mJ/cm^2}$, which coincides with a break in reflection and the onset of transmission. We interpret these effects as the onset of surface melting and we adopt the corresponding fluence value as the multi-shot threshold, F_N, which still includes incubation effects. For extrapolation to the single-shot damage fluence, F_1, we used the relation $F_N = F_1 N^{S-1}$, as proposed by Jee et al. [26], where N is the number of shots and S a parameter describing the degree of incubation. The closer S is to unity, the smaller the incubation. S can be obtained from the slope of a double logarithmic plot of NF_N against the total number of laser shots incurred at the multi-shot threshold [4, 12].

Such measurements were carried out on eleven Ni films of different thickness on fused silica substrates. The resulting threshold fluences are plotted in Fig. 8b. Again we observe the same general trend as in Fig. 7, but with the film thickness scaled down by a factor of about ten as a result of the $e-ph$ coupling strength for Ni being 15 times larger than that of Au (cf. Table 1). The solid line is a fit by TTM, this time with constant absorbed fluence. In Ni the d band is at the Fermi level, therefore transient changes in the reflectivity were less then 1%. The electron diffusion length indicated by the arrow is about 30 nm, which compared to Au is in agreement with the ratio $L_c(\mathrm{Ni})/L_c(\mathrm{Au})$. Note also that the saturation fluence of $22\,\mathrm{mJ/cm^2}$ for thick Ni samples is five times smaller than that for Au films, which reflects the higher energy density in the near-surface region of Ni. The damage threshold can be reduced even further for films with $d < 30\,\mathrm{nm}$. The results in Fig. 8b guarantee that the thermal damage zone is smaller than 50 nm when nickel is

[2] The fluence scale in [4] differs due to recalibration from the one shown here and in [12].

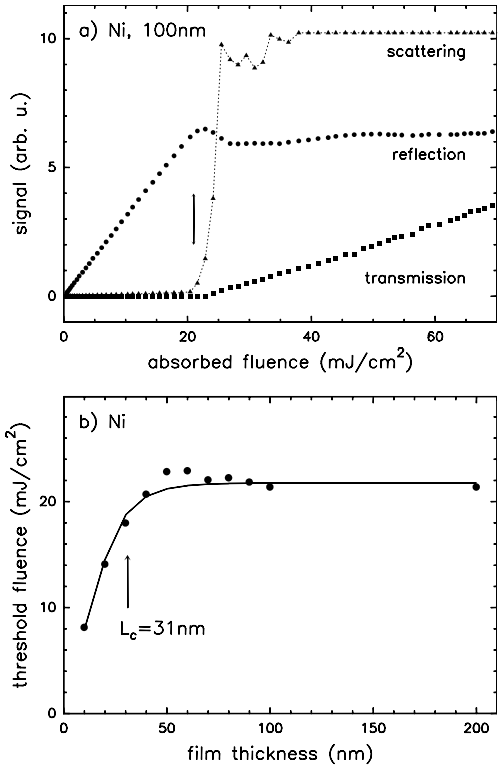

Fig. 8. a Detection of melting threshold of a 100-nm Ni film by measuring changes in scattering, reflection, and transmission of 400-nm, 200-fs laser pulses as a function of absorbed fluence. Each data point represents 7500 laser shots at the same spot. The *arrow* marks the multi-shot threshold. **b** Variation of single-shot melting thresholds with film thickness, obtained from measurements like the one shown in **a**. The *solid line* is a fit of the data by TTM and the *arrow* indicates the value for L_c

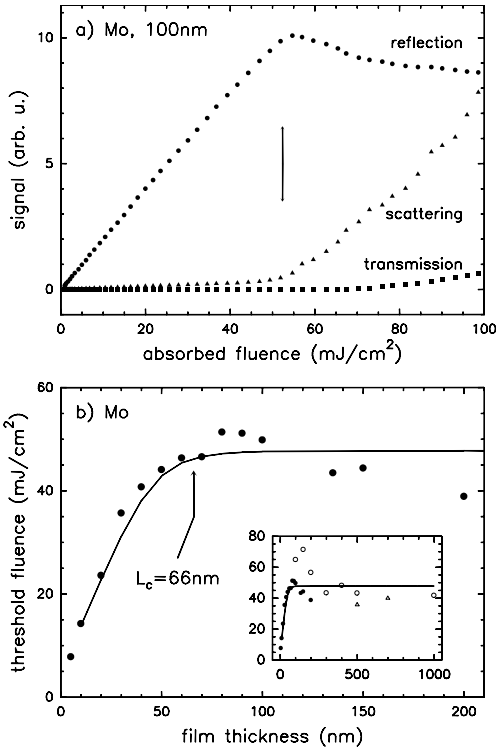

Fig. 9. a Changes in scattering and reflection of 400-nm, 200-fs laser pulses irradiating a 100-nm Mo film as a function of absorbed fluence. Each data point represents 7500 laser shots at the same spot. The *arrow* marks the multi-shot threshold. **b** Dependence of single-shot melting thresholds on film thickness with the arrow indicating L_c for Mo. The fit of the data by TTM treats the $e-ph$ coupling constant and the electronic heat capacity as free parameters. The *solid* and *open symbols* originate from different sample sets

microstructured with 200-fs or shorter pulses. The fact that the TTM describes the data well proves that, even for such ultrashort pulses, surface damage is still a purely thermal process.

Analogous experiments were carried out with Mo films on fused silica substrates [12]. A multi-shot fluence scan was made on one spot at room temperature in air. The change in the optical properties with fluence are shown in Fig. 9a, where again each data point represents the accumulated signal for 7500 shots. In comparison with the case for Ni films (see Fig. 8), the onset of scattering, marked by an arrow, is much less pronounced, but the change in reflectivity is similar. The combination of both yields a multi-shot threshold fluence which again can be reduced to a single-shot threshold, as described above (see also [12]).

Figure 9b displays the dependence of single-shot melting thresholds on the thickness of Mo films. We observe the same general trend as shown for Ni films in Fig. 8b, although the Mo data scatter more because the thresholds in Fig. 9a are not as distinct as those for Ni films. The reason for this is most likely the different thermoelastic properties of Mo films, which tend to fracture. The average saturation fluence of Mo is about twice as large as that for Ni. The solid line represents a TTM fit to the data with the $e-ph$ coupling constant and electronic heat capacities being free parameters. The results are listed in Table 1. The resulting $e-ph$ coupling strength is about 2.5 times smaller than the value for Ni. On the other hand, our result is about 6 times larger than the one reported by Corkum et al. [15] for Mo mirrors irradiated with 9.3-μm pulses of varying lengths. The satisfying agreement between our experimental data and model calculations again proves that damage of Mo by ultrashort pulses is a thermal process, which is surprising since the material is quite brittle.

Despite the uncertainties of the saturation thresholds and possible deviations between freestanding films and those on fused silica substrates because of thermoelastic effects, the data in Fig. 9b provide a guidance for microstructuring of Mo films. They indicate that the thermal damage layer is smaller than 50 nm. In future studies it would be desirable to complete the information by electron microscopy inspection of the damage topography for different film thickness.

2.3 Comparison of femtosecond and nanosecond laser damage as a function of film thickness

For technological applications it may be of interest to compare threshold fluences required for structuring metal films of different thickness with nanosecond or femtosecond pulses. This is done in Fig. 10 for Au and Ni films, where the single-shot threshold fluences for 248-nm, 14-ns pulses reported in [9] are plotted together with those obtained by using 400-nm, 200-fs pulses [4, 12]. Solid lines represent TTM fits,

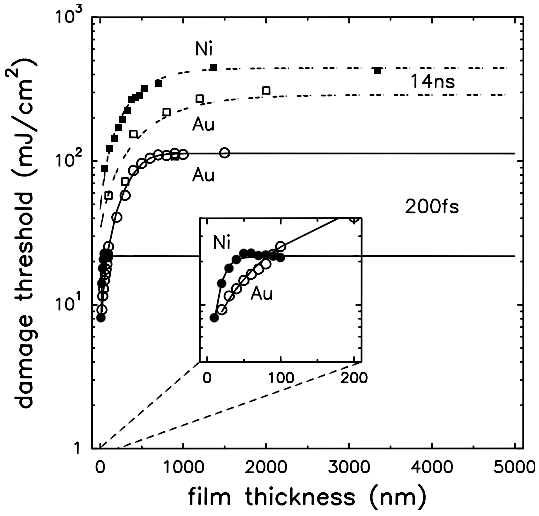

Fig. 10. Thickness dependence of damage thresholds measured with 248-nm, 14-ns and 400-nm, 200-fs laser pulses on Au and Ni films. Nanosecond data are taken from [9]. *Solid lines* represent fits by TTM and *dashed lines* those with the heat diffusion equation [11]. The *inset* magnifies the thickness scale to emphasize the threshold saturation for Ni films damaged with 200-fs laser pulses

dashed curves are calculations by using the common heat diffusion equation [11]. In this figure, three observations are of importance as follows.

(1) There is a dramatic reduction (a factor of 20) in the saturation (bulk) threshold of Ni when changing from nanosecond to subpicosecond pulses, in agreement with earlier reports by Preuss et al. [1][3]. In contrast, the difference for Au films amounts to only a factor of about three. This emphasizes the importance of $e-ph$ coupling, which in Ni films retains the absorbed energy density near the surface and prevents much diffusive loss to the interior.

(2) For the same reason, the electron diffusion range, defined in (9) as L_c, in Ni films is at least a factor of 30 shorter for femtosecond pulses than for nanosecond ones. This large difference is due to the fact that $e-ph$ coupling does not enter nanosecond laser melting but plays a major role in femtosecond laser damage. For Au films with weak $e-ph$ coupling, such a change is much less pronounced and amounts to only a factor of 3. This causes the thickness dependence of damage thresholds to be rather similar for nanosecond and femtosecond pulses.

(3) For both materials, however, we observe a strong decrease in the melting fluence with a decreasing film thickness for $d < L_c$. This effect offers the possibility to achieve contours with high edge precision and can be exploited for energy saving in the processing of metal films.

3 Summary

Threshold fluences for melting metal films by ultrashort laser pulses have been analyzed with the two-temperature model. Experimental data were presented for Au, Ni, and Mo films on fused silica substrates to provide a guidance for laser microstructuring of metals with femtosecond pulses and to demonstrate the different responses of noble and transition metals. For all three metals the variation of the melting fluence with the film thickness was measured in situ by observing the reflection, scattering, and transmission of the laser light. The experimental data were reduced to single-shot thresholds and fitted by TTM calculations, yielding the electron–phonon coupling strength. In the case of Au, the pulse length dependence of melting thresholds measured by Stuart et al. [3] was well reproduced by the TTM provided the transient absorption was taken into account.

These investigations lead to the following conclusions. (1) In contrast to the case with nanosecond pulses, electron–phonon coupling is important for femtosecond laser damage. It governs the diffusion length $L_c \propto (g)^{-1/2}$ of hot electrons and thereby determines the energy density near the surface. As a result, there are great differences in the threshold fluences for the melting of noble and transition metals. (2) Since melting requires a critical energy density, below the critical value L_c a decrease in the film thickness leads to a decrease in the damage threshold, which is analogous to the case with nanosecond pulses except at a reduced length scale. (3) The TTM is well capable of quantitatively modeling threshold fluences for damage. This result establishes that laser damage of metals, even with femtosecond lasers, is a purely thermal process. (4) For Au films, transient optical properties and ballistic energy transport must be accounted for in the source term, although electron diffusion is the dominant process. For laser melting of noble metals, ballistic transport is of minor importance and it can safely be neglected for transition metals, where its range does not exceed the optical absorption depth.

Acknowledgements. This work was supported by the Deutsche Forschungsgemeinschaft, Sonderforschungsbereich 290.

[3] The absolute fluence values reported in [1] differ from ours by about a factor of two.

References

1. S. Preuss, E. Matthias, M. Stuke: Appl. Phys. A **59**, 79 (1994)
2. S. Preuss, A. Demchuk, M. Stuke: Appl. Phys. A **61**, 33 (1995)
3. B.C. Stuart, M.D. Feit, S. Herman, A.M. Rubenchik, B.W. Shore, M.D. Perry: J. Opt. Soc. Am. B **13**, 459 (1996)
4. J. Güdde, J. Hohlfeld, J.G. Müller, E. Matthias: Appl. Surf. Sci. **127-129**, 40 (1998)
5. A. Semerok, C. Chaléard, V. Detalle, J.-L. Lacour, P. Mauchin, P. Meynadier, C. Nouvellon, B. Sallé, P. Palianov, M. Pedrix, G. Petite: Appl. Surf. Sci. **138-139**, 311 (1999)
6. S. Nolte, C. Momma, H. Jacobs, A. Tünnermann, B.N. Chichkov, B. Wellegehausen, H. Welling: J. Opt. Soc. Am. B **14**, 2716 (1997)
7. S. Nolte, C. Momma, B.N. Chichkov, H. Welling: Phys. Blätter **55**, 41 (1999)
8. M. Lenzner, J. Krüger, W. Kautek, F. Krausz: Appl. Phys. A **68**, 369 (1999)
9. E. Matthias, M. Reichling, J. Siegel, O.W. Käding, S. Petzoldt, H. Skurk, P. Bizenberger, E. Neske: Appl. Phys. A **58**, 129 (1994); and in *Laser Ablation: Mechanisms and Application-II*, ed. by J.C. Miller, D.B. Geohegan, AIP Conference Proceedings Vol. 288 (American Institute of Physics, New York 1994) p. 305
10. E. Matthias, J. Siegel, S. Petzold, M. Reichling, H. Skurk, O. Käding, E. Neske: Thin Solid Films **254**, 139 (1995)

11. J. Siegel, Ettrich, E. Welsch, E. Matthias: Appl. Phys. A **64**, 213 (1997); notice the printing error in (5) which should read:

$$F_c = \frac{T_f(z=0,\tau)L_f}{(1-R)}\frac{\varrho_f c_f}{(b-1)e^{-d/L_f}+(b+1)e^{d/L_f}} \times\left[(1+b)\left(e^{d/L_f}-1\right)+(1-b)\left(e^{-d/L_f}-1\right)\right] + \frac{T_f(z=0,\tau)L_s}{(1-R)}\frac{2\varrho_s c_s r}{(b-1)e^{-d/L_f}+(b+1)e^{d/L_f}}$$

12. S.-S. Wellershoff, J. Güdde, J. Hohlfeld, J.G. Müller, E. Matthias: SPIE **3343**, 378 (1998)
13. J. Hohlfeld, S.-S. Wellershoff, J. Güdde, U. Conrad, V. Jähnke, E. Matthias: Special Issue in Chemical Physics
14. J. Hohlfeld: *Ultrafast Electron-, Lattice- and Spin-Dynamics in Metals*, Dissertation, Freie Universität Berlin (Verlag für Wissenschaft und Forschung, Berlin 1998)
15. P.B. Corkum, F. Brunel, N.K. Sherman, T. Srinivasan-Rao: Phys. Rev. Lett. **61**, 2886 (1988)
16. W.S. Fann, R. Storz, H.W.K. Tom: J. Bokor: Phys. Rev. B **46**, 13592 (1992)
17. M. Aeschlimann, M. Bauer, S. Pawlik: Chem. Phys. **205**, 127 (1996)
18. M. Aeschlimann, M. Bauer, S. Pawlik, W. Weber, R. Burgmeister, D. Oberli, H.C. Siegmann: Phys. Rev. Lett. **79**, 5158 (1997)
19. C.-K. Sun, F. Valée, L.H. Acioli, E.P. Ippen, J.G. Fujimoto: Phys. Rev. B **50**, 15337 (1994)
20. C. Suárez, W.E. Bron, T. Juhasz: Phys. Rev. Lett. **75**, 4536 (1995)
21. J. Hohlfeld, J.G. Müller, S.-S. Wellershoff, E. Matthias: Appl. Phys. B **64**, 387 (1997)
22. S.I. Anisimov, B. Kapeliovich, T. Perel'man: Sov. Phys. JETP **39**, 375 (1974)
23. J.H. Bechtel: J. Appl. Phys. **46**, 1585 (1975)
24. M. von Allmen: *Laser-Beam Interactions with Materials*, Springer Series in Materials Science, Vol. 2 (Spinger, Berlin, Heidelberg 1987)
25. S. Petzoldt: *Der Einfluß intensiver Laserpulse auf Metalloberflächen: Vom Heizen bis zum laserinduzierten Plasma, beobachtet mit dem akustischen "Mirage-Effekt"*, Dissertation, Freie Universität Berlin (Verlag Dr. Köster, Berlin 1995)
26. Y. Jee, M.F. Becker, R.M. Walser: J. Opt. Soc. Am. B **5**, 648 (1988)
27. D.E. Gray (Ed.): *American Institute of Physics Handbook*, 3rd ed. (McGraw-Hill, New York 1972)
28. A.M. James, M.P. Lord: *Maxmillan's Chemical and Physical Data* (Maxmillan Press, London 1992)